Article:

Multi-faceted machine learning of competing orders in disordered interacting systems

Michael Matty[1],[*] Yi Zhang[1], Zlatko Papić[2], and Eun-Ah Kim[1][†]

[1]*Department of Physics, Cornell University, Ithaca, New York 14853, USA and*
[2]*School of Physics and Astronomy, University of Leeds, Leeds LS2 9JT, UK*

(Dated: September 21, 2019)

While the non-perturbative interaction effects in the fractional quantum Hall regime can be readily simulated through exact diagonalization, it has been challenging to establish a suitable diagnostic that can label different phases in the presence of competing interactions and disorder. Here we introduce a multi-faceted framework using a simple artificial neural network (ANN) to detect defining features of a fractional quantum Hall state, a charge density wave state and a localized state using the entanglement spectra and charge density as independent input. We consider the competing effects of a perturbing interaction ($l = 1$ pseudopotential ΔV_1), a disorder potential W, and the Coulomb interaction to the system at filling fraction $\nu = 1/3$. Our phase diagram benchmarks well against previous estimates of the phase boundary along the axes of our phase diagram where other measures exist. Moreover, exploring the entire two-dimensional phase diagram for the first time, we establish the robustness of the fractional quantum Hall state and map out the charge density wave micro-emulsion phase wherein droplets of charge density wave region appear before the charge density wave is completely disordered. Hence we establish that the ANN can access and learn the defining traits of topological as well as broken symmetry phases using multi-faceted inputs of entanglement spectra and charge density.

I. INTRODUCTION

Using the fact that neural network based machine learning can effectively distill relevant information and compactly represent a complex function, there have been recent efforts to efficiently (i) obtain phase diagrams [1–20] and (ii) represent wave functions [6,12,21–29] of many-body quantum systems. Machine learning based phase detection is a particularly promising direction for phases outside the traditional "knowledge compression scheme" – the local order parameter. Topological phases form a central class of such phases. Though there has been recent progress in using machine learning for topological phases [3,4,9,12,15,19,30,31], these early efforts naturally centered around benchmarking the neural network based approaches to the conventional approaches on established problems by suppressing either disorder or interaction.

Here we turn to a strongly interacting two-dimensional electron gas (2DEG) in the fractional quantum Hall regime. 2DEG hosts a rich phase diagram in which topological order in various quantum Hall states competes against various forms of spontaneously broken symmetries. All this can only be observed in clean samples, which abundantly speaks to the key role of disorder. Such competition among interaction driven correlated states and disorder driven localized states is a common theme of all strongly correlated systems. Yet, 2DEG forms the simplest system in which such competition can be studied experimentally, with the magnetic field quenching the kinetic energy. Nevertheless theoretical study is challenging since the traditional diagnostic of the fractional quantum Hall state requires translational symmetry.

Previous works[32–35] on the effect of disorder on the FQH effect focused on establishing a measure that can assess the robustness of the topological order. This was already a challenging task because most measures of topological order are naturally suited to uniform systems with translation invariance. The resulting measures of the total Chern number[32,33] and the slope of the entanglement entropy as a function of average disorder strengths[34,35] are compelling. Nevertheless, they are computationally costly. More importantly, these measures are mostly geared towards a bi-partite phase diagram consisting of a FQH state and a localized, insulating state (for example, the quantization of the Chern number would not distinguish between different incompressible phases realized at the same filling factor). Here we study the problem including *both* disorder and a competing interaction from two complementary perspectives: the entanglement spectrum (ES) and the real space charge density (CD).

Motivated by the fruitful use of entanglement spectra in clean systems with topological order[36–38], efforts sought indication of the robustness of the topological state within the entanglement spectrum in the presence of disorder [34,35,39]. The ES $\{\xi_i\}$ is a set of eigenvalues of the reduced density matrix, characterizing a subsystem of a quantum system[36]. Traditionally, the levels in the ES are organized according to a symmetry quantum number (typically, linear or angular momentum), which reveals characteristic structures in translationally invariant systems. However, such an organizing principle is lost with the introduction of disorder, and one must resort to studying the *distribution* of the entanglement spectrum levels as previously used, e.g., in the studies of many-body localization[40,41]. Alternatively, the real space charge density provides a two-dimensional image of the wave function that can characterize phases through its spatial profile. However, in the presence of interactions it becomes non-trivial to assign phase boundaries simply from images of the charge density. Thus, competing interactions and disorder necessitate an approach that can discover distinguishable structure in multiple

facets: the ES and the CD.

In this paper we use supervised machine learning on ES and CD to obtain the phase diagram of three competing phases tuned by interaction and disorder strength: FQH, charge density wave (CDW), and a localized state. This approach is versatile and numerically efficient. It can be generalized to incorporate other phases, system geometries, and disorder models. We start by briefly reviewing the standard theoretical model for the FQH system in the presence of Gaussian white noise disorder in Sec. II. In Sec. III we introduce our method based on ANN. Our results are presented in Sec. IV. We conclude with a summary of our results and open questions in Sec. V.

II. MODEL

We consider a system of electrons on a torus in the presence of a magnetic field, see Fig. 1. The area of the torus $\mathcal{A}$ is set by the magnetic flux, $\mathcal{A} = 2\pi\ell_B^2 N_\phi$ in units of the magnetic area $2\pi\ell_B^2$, where $\ell_B = \sqrt{\hbar/eB}$ is the magnetic length. We set the aspect ratio of the torus to be unity, corresponding to a square unit cell with periodic boundary conditions. The electron density is held fixed at one electron per three magnetic fluxes, i.e., the filling fraction is $\nu = 1/3$.
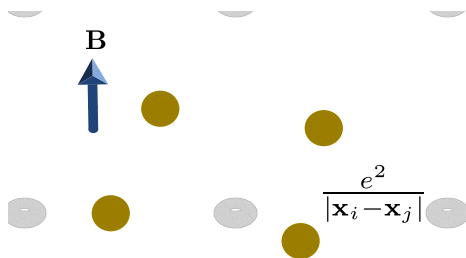

FIG. 1. Two-dimensional electron gas on a torus with perpendicular magnetic field B. Electrons interact via the Coulomb potential in Eq. (2), while the grainy surface of the torus depicts the presence of Gaussian white noise disorder, Eq. (5). The partitioning of the system into parts A and B, used to define the entanglement spectrum, is also indicated.

The system is described by the Hamiltonian

$$H = H_0 + H_{\text{pert}}, \tag{1}$$

where H_0 represents the Coulomb interaction between the electrons,

$$H_0 = \sum_{i<j} \frac{e^2}{|\mathbf{x}_i - \mathbf{x}_j|}, \tag{2}$$

and the $\mathbf{x}_i$'s denote the positions of the electrons in the 2D plane. We emphasize that all the terms in the Hamiltonian are explicitly projected to the lowest Landau level

using standard techniques[42,43]. Physically, this corresponds to taking the limit of an infinite magnetic field, which is an excellent approximation for most purposes[43]. In addition to the Coulomb potential, we consider two physical perturbations:

$$H_{\text{pert}} = H'(\Delta V_1) + H_{\text{imp}}(W). \tag{3}$$

where H' denotes the perturbation by a short-range (contact) interaction between the electrons,

$$H'(\Delta V_1) = \Delta V_1 \sum_{i<j} \nabla_i^2 \delta(\mathbf{x}_i - \mathbf{x}_j), \tag{4}$$

also known as the Haldane V_1 pseudopotential[44]. The strength of this perturbation is denoted by the overall prefactor ΔV_1. Physically, this perturbation could arise due to effects of finite thickness of the 2D electron gas, excitations to other Landau levels, etc. On the other hand, the quenched disorder potential is denoted by a (one-body) term $H_{\text{imp}}(W)$. We model disorder as Gaussian white noise[33] randomly distributed with mean value 0 and width W in real space, i.e.

$$\langle H_{\text{imp}}(W, \mathbf{x})\rangle = 0, \tag{5}$$

$$\langle H_{\text{imp}}(W, \mathbf{x})H_{\text{imp}}(W, \mathbf{x}')\rangle = W^2 \delta(\mathbf{x} - \mathbf{x}'). \tag{6}$$

The important feature for our purposes, which is shared with other common disorder models such as finite-range scatterers or correlated impurity potentials, is that the disorder potential breaks magnetic translation invariance, thus we do not have a good quantum number to classify the many-body states.

We anticipate three phases in the parameter space $(W, \Delta V_1)$ of the above model. First, we expect the Laughlin $\nu = 1/3$ FQH state[45] in the absence of H' and H_{imp}[46]. Second, decreasing the V_1 pseudopotential lowers the energy of the finite wave vector magnetoroton excitation[47], driving a transition to a topologically trivial CDW state at large enough $-|\Delta V_1|$[46]. Finally, increasing the characteristic strength of the disorder W eventually leads to a localized state[33]. Nevertheless, mapping out the phase diagram in the space of $(W, \Delta V_1)$ with these competing tendencies requires not only a numerical study but more importantly a new diagnostic.

III. METHOD

We use an artificial neural network (ANN) to diagnose structures in the ES and CD data characteristic of each phase. To obtain the ES and CD data, we exactly diagonalize the full Hamiltonian in Eq. (1) for each point in the two-dimensional parameter space $(W, \Delta V_1)$ and each disorder configuration. The CD, $\rho(\mathbf{x}) = \langle\psi|\hat{\Psi}^\dagger(\mathbf{x})\hat{\Psi}(\mathbf{x})|\psi\rangle$ with the electron field operator $\hat{\Psi}(\mathbf{x})$, is an obvious choice for detecting CDW state. To form the input we evaluate the density $\rho(\mathbf{x})$ on a 20×20 mesh of evenly spaced points $\mathbf{x}$. This is then passed to our ANN as a vectorized two-dimensional image.
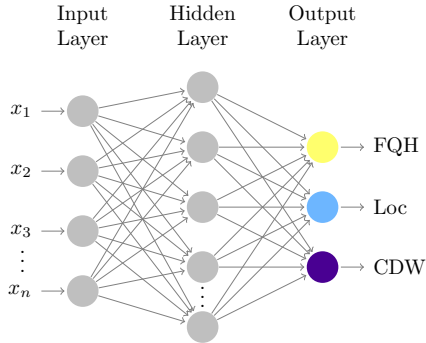
FIG. 2. Schematic diagram of neural network. We use the rank ordered entanglement spectrum or the charge density as input x_i. The hidden layer is specified by weights w_{ij} and biases b_i. We use a single hidden layer in the case of the rank ordered entanglement spectrum, and two in the case of the charge density. Each output neuron corresponds to a phase under consideration, with the output value the neural network's judgement on the likelihood of the phase. We normalize outputs using a softmax layer.

Our choice of inspecting the CDW-Localization transition through ES is motivated by the distinct scaling of entanglement entropy anticipated in the two phases[48]. From each of the three lowest energy many-body eigenstates (which are topologically degenerate in the FQH phase), $|\psi\rangle$, we obtain the bi-partite ES, $\{\xi_i\}$, by partitioning the system in the orbital space[36] , as indicated in Fig. 1. We note that, because of Gaussian localization of single-particle orbitals in a Landau level, the partitioning in orbital space roughly corresponds to an actual partition in real space. Having fixed the choice of the partition, we then perform the standard Schmidt decomposition $|\psi\rangle = \sum_i e^{-\xi_i/2}|A_i\rangle|B_i\rangle$, where the vectors $|A_i\rangle$ form an orthonormal basis for the subsystem A (and similarly for subsystem B).[49] The ES input for our ANN's is simply a rank ordered list of numbers ξ_i.[50]

The architecture of our choice is a fully-connected feedforward artificial neural network with a single hidden layer containing 100 neurons for processing the ES data, and two hidden layers with 200 and 50 neurons for the CD data, see Fig. 2.[51] Each neuron j processes the inputs x_i according to the weight matrix w_{ji} and the bias vector b_j specific to that neuron $\sigma(w_{ji}x_i + b_j)$ where the rectified linear activation function is given by $\sigma(y) \equiv \max(y, 0)$. The sum of the neural outputs is normalized via a softmax layer.

Given the theoretical insight, we train the neural network using data from 5000 disorder configurations at one training point deep inside each phase (chosen in an appropriate parameter regime with high training accurcy). When charge density is used as an input we put the training points $(W^t, -\Delta V_1^t)$ at $(10^{-6}, 0)$ for the FQH state,

$(0.2, 0)$ for the localized state, and $(10^{-6}, 0.2)$ for the CDW state. Because the ES did not diversify enough with such low disorder strength, we move the training point for FQH to $(0.05, 0)$. We use cross-entropy as the cost function for stochastic gradient descent. Once the network is trained to $> 99\%$ accuracy, we fix the weights and biases and let the ANN recognize the phase associated with the rest of the phase space by averaging the neuron outputs from 500 disorder configurations for each phase space point.

IV. RESULTS

Our multifaceted approach reveals new insight into the characteristics of topological, symmetry-breaking, and localized phases and their competition. The full phase diagram is shown in Fig. 3. This phase diagram was obtained for the system with $N = 5$ electrons, with NN training points indicated by red crosses, the red circle, and the red triangle. Although the lack of symmetry prevents one from reaching large system sizes, we note that qualitatively similar phase diagrams are obtained for other values of N. The phase diagram contains four distinct regions that have been labelled in Fig. 3. In order to construct this plot we separately take the phase diagram obtained by using the CD and ES as input to the ANN. Then, to highlight the differences in the output for $-\Delta V_1 > 0.1$, we decrease the opacity of the CD output by 50% and layer it over the ES output. In order to develop some intuition behind the identification of these phases, it is instructive to also inspect the typical (i.e. from a single, arbitrary disorder configuration) CD and ES in each of the regions in the phase diagrams, which are shown in Figs. 4 and 5, respectively. We next discuss in detail each of the four phases in the diagram, and their transitions to neighboring phases.

A. Identification of phases

First, we identify a robust region corresponding to topological order of the Laughlin $\nu = 1/3$ state, indicated by the yellow color in Fig. 3, using ES as input for $-\Delta V_1 < 0.1$. As the Laughlin state represents an incompressible liquid, we expect its CD to be spatially uniform in the absence of disorder, as indeed confirmed by Fig. 4(a). Furthermore, as the Laughlin phase is a *gapped* liquid, it remains stable for some finite amount of perturbations, either by softening of the interactions $(-|\Delta V_1|)$ or by disorder W.

In the clean limit $(W \ll 1)$, the system is expected to undergo a quantum phase transition from the FQH phase into a CDW phase upon increasing the magnitude of the V_1 pseudopotential perturbation $-|\Delta V_1|$[43]. Indeed, we can see in Fig. 3 that for weak disorder $(W = 10^{-6})$ and sufficiently negative $-|\Delta V_1| = 0.2$, the ANN finds a phase transition based on both CD and ES facets of the
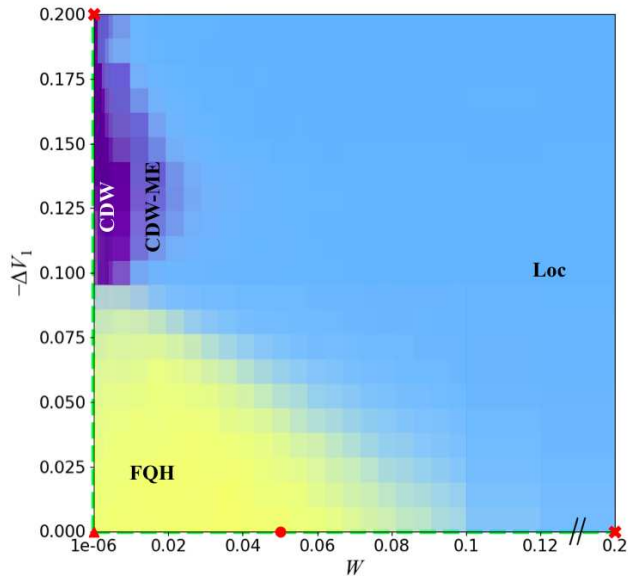
FIG. 3. The phase diagram based on the output from three output-neuron neural network. Black slashes mark an axis break. Red x's mark training points used when using the ES or the CD as input. The red circle marks a training point used when only the ES is used as input, a red traingle marks that utilized only for the CD input. Cuts along the two axes(emphasized with green dashed lines) are shown in Figs. 6 and 7, respectively. Outputs of each neuron scale from transparent to opaque as output goes from zero to one. We decrease the opacity of the output obtained using the CD by 50%, and layer it over the output obtained using the ES above the $-\Delta V_1 = 0.1$ line

.

data. The plot of the charge density in the large $-|\Delta V_1|$ region Fig. 4(a) clearly shows a stripe CDW phase.

We now turn to the light purple region of Fig. 3 at intermediate disorder strength. At moderate disorder strength of $W_{c1} \lesssim 0.01$, the long-range CDW (i.e., correlation length of the order of the system size) is destroyed. Here the two facets of the data, CD and ES give us different insights. From the CD facet, the formation of large droplets as shown in Fig. 4(c) is recognized by the ANN to be similar to the CD distribution of localized phase in Fig. 4(d). But clearly the distribution of charge in Fig. 4(c) is more organized to the extent that it is somewhat reminiscent of a crystalline CDW bubble phase[52-54] that is usually discussed in the context of clean, fractionally filled higher Landau levels. However, considering the boundary conditions, the CD only exhibits two droplets and does not really match the description of a crystalline state with multiple electrons per site.

Further insight into this light purple region is afforded by looking at the ES facet. While the ANN assessment of the region based on the CD data was to identify it with the localized phase, this changes when the ES data is given. Actually, the ANN looking at the ES data identifies this region with the CDW phase. Looking at the

plot of typical rank-ordered entanglement spectra shown in Fig. 5 it is clear that the ES of this intermediate disorder regime is distributed in a fashion quite similar to that of the CDW phase, especially at low entanglement energies. Hence, the comparison between the ANN assessment based on CD and that based on ES is that this region shares characteristics of both a heterogeneous state and a CDW state.

According to the Imry-Ma argument[55], the CDW order is expected to first break into droplets of CDW states of correlation length smaller than the system size. Although the stripe pattern is invisible in the CD distribution of this region in Fig. 4(c) due to the resolution of our calculation, the fact that the size of the droplets are such that they can contain several CDW wavelengths makes it plausible that the purple region is supporting a CDW-microemulsion (CDW-ME) rather than a featureless localized state. A new finding is that ANN can distinguish this state from a localized state, which is realized at even stronger disorder [see Fig. 4(d)], based on the ES facet. Our ANN is finding the ES structure of this CDW-ME to be identifiable as that of the long-range CDW state, while the CD structure of the CDW-ME to be identifiable as that of localized state. This identification of the CDW-ME is a new diagnostic afforded by our multifaceted application of ANN.
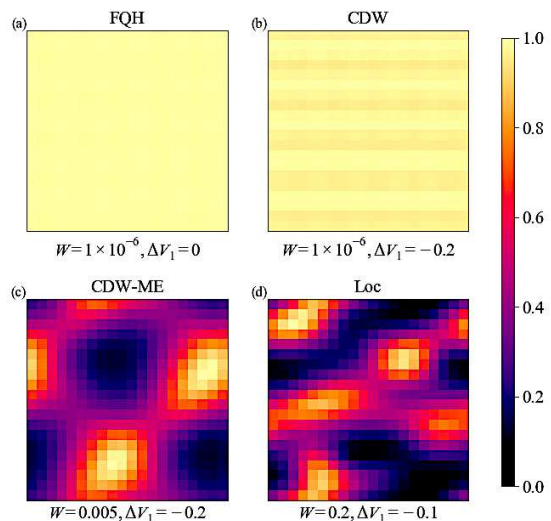

FIG. 4. Typical real space charge density profiles $\rho(\mathbf{x})$ in (a) the FQH phase, (b) the CDW phase, (c) the intermediate CDW-ME state, and (d) the localized state. In each case the charge density is plotted as a fraction of the maximum value it attains on the torus, and colorized as shown in the color bar on the right. The charge density is largely uniform in the FQH phase, exhibits stripes in the CDW phase, separated "droplets" in the CDW-ME phase, and is seemingly random in the localized state.
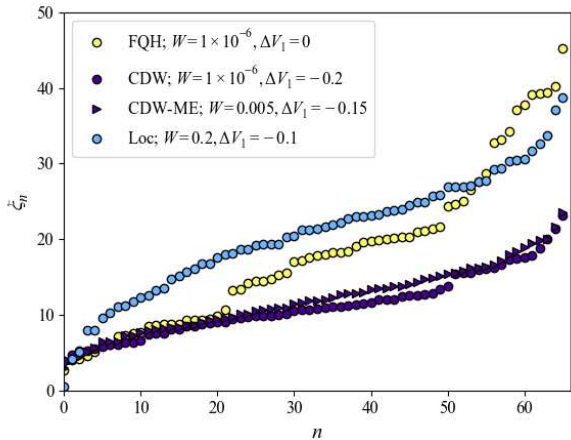
to a good quantum number or the charge density.

FIG. 5. Typical entanglement spectra in each of the four phases identified in Fig. 3. The entanglement energies ξ_n are plotted against their indices n in the rank-ordered entanglement spectrum. We observe that the ES are visually distinct between the FQH, localized, and CDW states. However, the CDW-ME looks comparatively similar to the CDW from the ES perspective, especially in the lower entanglement energy part of the ES.

B. Phase transitions

We now examine in detail the transitions between the phases by studying one-parameter slices of our phase diagram in Fig. 3. This will provide us with further benchmarks against some results that are available in the literature, which have been obtained via more conventional diagnostics of quantum phase transitions varying only one of the two parameters of our phase space.

In the clean limit, a transition between a CDW phase and an FQH state is known to occur as a function of ΔV_1[43]. The cut along the ΔV_1 axis is shown in Fig. 6(a), and it indeed reveals a sharp transition between the FQH output dominant region and the CDW output dominant region around $-\Delta V_1 \approx 0.1$. It is illuminating to contrast this neural network based detection of the phase transition to the conventional measures such as the wave function overlap with the Laughlin state, which is shown in Fig. 6(b). We observe that the overlap drops sharply to near zero at around the same value $-\Delta V_1 \approx 0.1$ as well. Note that because we still have very weak but non-zero disorder ($W = 10^{-6}$) in Fig. 6, we present the overlap between equal amplitude superpositions of the three topologically degenerate Laughlin states and the three lowest energy eigenstates of the exact Hamiltonian, which are topologically degenerate in the FQH phase. The remarkable agreement between different diagnostics of the transition suggests that our neural network can accurately distinguish competing phases that are not related by symmetry, solely based on either the rank-ordered entanglement spectrum without reference
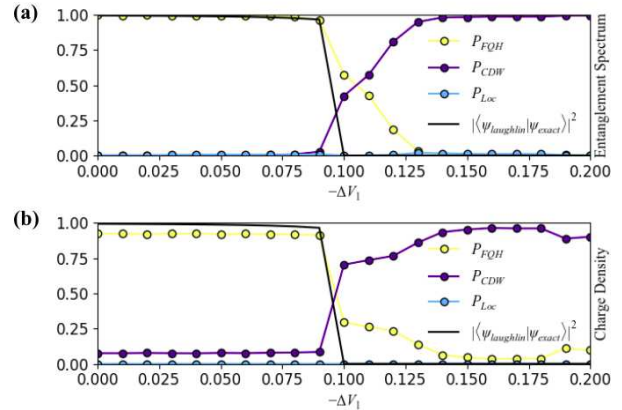

FIG. 6. (a) The FQH-CDW transition along $W = 1 \times 10^{-6}$. Neural network output for probabilities of the system being in the FQH, CDW, and localized states (P_{FQH},P_{CDW}, and P_{Loc}, respectively) as a function of pseudopotential shift ΔV_1 for $N_e = 5$ using the ES (upper panel) and (b) the CD (lower panel) as input to the ANN. Phase transition to CDW is predicted around $\Delta V_1 = -0.1$. (b) The overlap between the Laughlin state and the exact ground state of the Hamiltonian. Precipitous drop in overlap also predicts phase transition around $\Delta V_1 = -0.1$.

Finally, we turn to the localization transition along the W axis and pure Coulomb interaction ($\Delta V_1 = 0$). The $\Delta V_1 = 0$ cut shown in Fig. 7 shows a broad transition around $W_c \approx 0.095$. Unlike the CDW transition in the clean case, however, there is no rigorously established conventional criteria for this localization transition. Liu and Bhatt[34,35] have recently proposed tracking the finite-size scaling of the numerical derivative of the ground state entanglement entropy with respect to disorder strength, dS/dW. This diagnostic (also used in Ref. 56 for a bilayer quantum Hall system) puts the threshold at a much smaller disorder strength of $W \approx 0.09$, which is in good agreement with our resuls.

V. CONCLUSIONS

We have used supervised machine learning via ANN to study the disorder-interaction phase diagram involving three competing states: FQH, CDW, and localized state. Using multiple facets of the data (rank-ordered ES and CD), we have reproduced known results along the two axes of the phase diagram. In the weak disorder limit ($W \lesssim 0.01$), the ANN finds the phase transition between the FQH phase and the CDW phase around $\Delta V_1 \approx -0.1$, which agrees with other estimates of the transition based on wave function overlap. In the Coulomb interaction limit ($\Delta V_1 = 0$), the ANN finds the FQH phase to localize around disorder strength $W \approx 0.095$.

Furthermore, we have extended the previous results to the full two-dimensional ($W, -\Delta V_1$) phase diagram. We
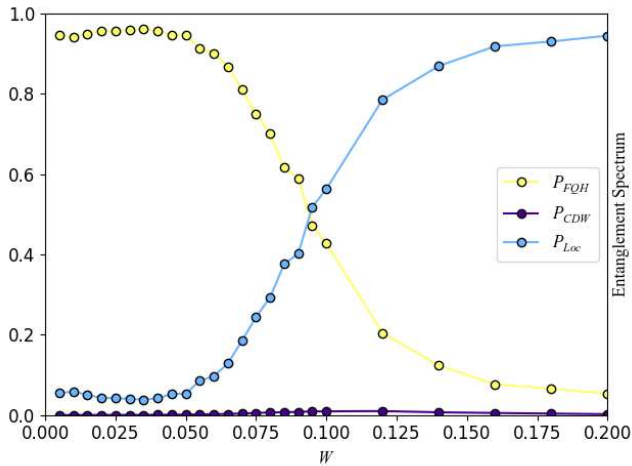
FIG. 7. The FQH-localized state transition at $\Delta V_1 = 0$. Neural network output probabilities of the system being in the FQH, CDW, and localized states (P_{FQH}, P_{CDW}, and P_{Loc} respectively) as a function of disorder strength W for $N_e = 5$ observed over $W \in [10^{-6}, 0.2]$ using the ES as input to the ANN. Phase transition to the localized state is predicted around $W = 0.095$.

found the FQH phase to be more robust to the disorder than CDW, as is expected from the fact that FQH is a topologically ordered state and CDW should be sensitive to disorder. At the same time, using the rank-ordered ES and CD as two independent facets of the computational data revealed the new regime of CDW-ME which has droplets of CDW with CDW correlation length less than the system size that nevertheless has the same entanglement structure as the CDW phase.

Our study also shows that the ES can serve as a diagnostic of phase transitions in the case of competing interaction and disorder when the relevant phases are distinguished by entanglement properties, even in the absence of a traditional organizing principle for the ES. Moreover we have seen that the ES contains structure that understands the formation of multiple CDW droplets as being similar to a single CDW, as opposed to just recognizing symmetry breaking.

A distinct advantage of the ML method is its numerical efficiency: it only requires a large number of disorder configurations at the points of neural network training, whereas interpolation can be performed by averaging

over far fewer (e.g. 500 at each interpolation point compared to several thousand at each training point). There is also no need to search through the entirety of parameter space to locate a phase transition: it is found directly by interpolating between the neural network training points. This is especially advantageous in the case of a multidimensional parameter space. Note also that this method is not tied to any particular system geometry or disorder model. When studying the ground state of systems with competing interactions and disorder, the success of supervised machine learning in studying transitions between the FQH, CDW, and localized states supports the search for diagnostic quantities that distinguish the relevant phases that can be understood via machine learning without needing to be understood by humans.

As a subject of future work, we would also like to explore experimental applications of our technique. To this end, we propose the application of our method to another type of experimentally accessible input data: Fock space data from ultra cold lattice gas experiments (see for example ref.[57]). Near-term experiments hope to realize FQH states in cold atom systems[58–64], but the diagnosis of these states remains challenging. This is due to the lack of a human-interpretable feature in the Fock space data that can distinguish the FQH states from other nearby phases. We propose to use our ML technique to learn the relevant structure from the Fock space data to aid in the diagnosis of FQH phases.

VI. ACKNOWLEDGEMENTS

[*] mfm94@cornell.edu

[†] eun-ah.kim@cornell.edu

[1] P. Broecker, J. Carrasquilla, R. G. Melko, and S. Trebst, Scientific Reports **7**, 8823 (2017).

[2] P. Broecker, F. F. Assaad, and S. Trebst, arXiv preprint (2017).

[3] Y. Zhang and E.-A. Kim, Phys. Rev. Lett. **118**, 216401 (2017).

[4] Y. Zhang, R. G. Melko, and E.-A. Kim, Phys. Rev. B **96**, 245119 (2017).

[5] L. Wang, Phys. Rev. B **94**, 195105 (2016).

[6] G. Carleo and M. Troyer, Science **355**, 602 (2017).

[7] J. Carrasquilla and R. G. Melko, Nature Physics **13**, 431 EP (2017).

[8] E. P. L. van Nieuwenburg, Y.-H. Liu, and S. D. Huber, Nature Physics **13**, 435 EP (2017).

[9] M. J. S. Beach, A. Golubeva, and R. G. Melko, Phys. Rev. B **97**, 045207 (2018).

[10] K. Ch'ng, J. Carrasquilla, R. G. Melko, and E. Khatami, Phys. Rev. X **7**, 031038 (2017).

[11] K. Ch'ng, N. Vazquez, and E. Khatami, Phys. Rev. E **97**, 013306 (2018).

[12] D.-L. Deng, X. Li, and S. Das Sarma, Phys. Rev. B **96**, 195145 (2017).

[13] Y.-H. Liu and E. P. L. van Nieuwenburg, Phys. Rev. Lett. **120**, 176401 (2018).

[14] E. van Nieuwenburg, E. Bairey, and G. Refael, Phys. Rev. B **98**, 060301 (2018).

[15] T. Ohtsuki and T. Ohtsuki, Journal of the Physical Society of Japan **85**, 123706 (2016).

[16] F. Schindler, N. Regnault, and T. Neupert, Phys. Rev. B **95**, 245134 (2017).

[17] S. J. Wetzel and M. Scherzer, Phys. Rev. B **96**, 184410 (2017).

[18] S. J. Wetzel, Phys. Rev. E **96**, 022140 (2017).

[19] N. Yoshioka, Y. Akagi, and H. Katsura, Phys. Rev. B **97**, 205110 (2018).

[20] J. Venderley, V. Khemani, and E.-A. Kim, Phys. Rev. Lett. **120**, 257204 (2018).

[21] Z. Cai and J. Liu, Phys. Rev. B **97**, 035116 (2018).

[22] J. Chen, S. Cheng, H. Xie, L. Wang, and T. Xiang, Phys. Rev. B **97**, 085104 (2018).

[23] D.-L. Deng, X. Li, and S. Das Sarma, Phys. Rev. X **7**, 021021 (2017).

[24] X. Gao and L.-M. Duan, Nature Communications **8**, 662 (2017).

[25] Y. Huang and J. E. Moore, ArXiv preprint arXiv:1701.06246 (2017).

[26] J. Liu, Y. Qi, Z. Y. Meng, and L. Fu, Phys. Rev. B **95**, 041101 (2017).

[27] Y. Nomura, A. S. Darmawan, Y. Yamaji, and M. Imada, Phys. Rev. B **96**, 205152 (2017).

[28] M. Schmitt and M. Heyl, SciPost Phys. **4**, 013 (2018).

[29] G. Torlai, G. Mazzola, J. Carrasquilla, M. Troyer, R. Melko, and G. Carleo, Nature Physics **14**, 447 (2018).

[30] N. Sun, J. Yi, P. Zhang, H. Shen, and H. Zhai, Phys. Rev. B **98**, 085402 (2018).

[31] P. Zhang, H. Shen, and H. Zhai, Phys. Rev. Lett. **120**, 066401 (2018).

[32] D. N. Sheng, X. Wan, E. H. Rezayi, K. Yang, R. N. Bhatt, and F. D. M. Haldane, Phys. Rev. Lett. **90**, 256802 (2003).

[33] X. Wan, D. N. Sheng, E. H. Rezayi, K. Yang, R. N. Bhatt, and F. D. M. Haldane, Phys. Rev. B **72**, 075325 (2005).

[34] Z. Liu and R. N. Bhatt, Phys. Rev. B **96**, 115111 (2017).

[35] Z. Liu and R. N. Bhatt, Phys. Rev. Lett. **117**, 206801 (2016).

[36] H. Li and F. D. M. Haldane, Phys. Rev. Lett. **101**, 010504 (2008).

[37] R. Thomale, A. Sterdyniak, N. Regnault, and B. A. Bernevig, Phys. Rev. Lett. **104**, 180502 (2010).

[38] X.-L. Qi, H. Katsura, and A. W. W. Ludwig, Phys. Rev. Lett. **108**, 196402 (2012).

[39] E. Prodan, T. L. Hughes, and B. A. Bernevig, Phys. Rev. Lett. **105**, 115501 (2010).

[40] S. D. Geraedts, R. Nandkishore, and N. Regnault, arXiv preprint (2016).

[41] M. Serbyn, A. A. Michailidis, D. A. Abanin, and Z. Papić, Phys. Rev. Lett. **117**, 160601 (2016).

[42] G. Fano, F. Ortolani, and E. Colombo, Phys. Rev. B **34**, 2670 (1986).

[43] R. E. Prange and S. M. Girvin, Springer-Verlag (1990).

[44] F. D. M. Haldane, Phys. Rev. Lett. **51**, 605 (1983).

[45] R. B. Laughlin, Phys. Rev. Lett. **50**, 1395 (1983).

[46] F. D. M. Haldane and E. H. Rezayi, Phys. Rev. Lett. **54**, 237 (1985).

[47] S. M. Girvin, A. H. MacDonald, and P. M. Platzman, Phys. Rev. B **33**, 2481 (1986).

[48] M. A. Metlitski and T. Grover, arXiv preprint (2015).

[49] Note that the von Neumann (entanglement) entropy can be directly computed from $\{\xi_i\}$ via the expression $S = \sum_i \xi_i e^{-\xi_i}$.

[50] We do not consider reduced density matrix eigenvalues below numerical precision, instead setting the corresponding ξ_i to zero.

[51] We have also considered a convolutional neural network, but found that it achieves comparable results but takes longer to train, so we used the simpler, feed-forward network instead.

[52] A. A. Koulakov, M. M. Fogler, and B. I. Shklovskii, Phys. Rev. Lett. **76**, 499 (1996).

[53] R. Moessner and J. T. Chalker, Phys. Rev. B **54**, 5006 (1996).

[54] F. D. M. Haldane, E. H. Rezayi, and K. Yang, Phys. Rev. Lett. **85**, 5396 (2000).

[55] Y. Imry and S.-k. Ma, Phys. Rev. Lett. **35**, 1399 (1975).

[56] J. Schliemann, Phys. Rev. B **83**, 115322 (2011).

[57] A. Mazurenko, C. S. Chiu, G. Ji, M. F. Parsons, M. Kanász-Nagy, R. Schmidt, F. Grusdt, E. Demler, D. Greif, and M. Greiner, Nature **545**, 462 EP (2017).

[58] M. Hafezi, A. S. Sørensen, E. Demler, and M. D. Lukin, Phys. Rev. A **76**, 023613 (2007).

[59] N. R. Cooper and J. Dalibard, Phys. Rev. Lett. **110**, 185301 (2013).

[60] G. Möller and N. R. Cooper, Phys. Rev. Lett. **103**, 105303 (2009).

[61] C. Nayak, S. H. Simon, A. Stern, M. Freedman, and S. Das Sarma, Rev. Mod. Phys. **80**, 1083 (2008).

[62] R. N. Palmer and D. Jaksch, Phys. Rev. Lett. **96**, 180407 (2006).

[63] A. S. Sørensen, E. Demler, and M. D. Lukin, Phys. Rev. Lett. **94**, 086803 (2005).

[64] A. Sterdyniak, B. A. Bernevig, N. R. Cooper, and N. Regnault, Phys. Rev. B **91**, 035115 (2015).

Here we briefly demonstrate the robustness of our results to changes in system size by reproducing figures 7 and 6 for $N_e = 6$. Here we consider the ES input for simplicity.
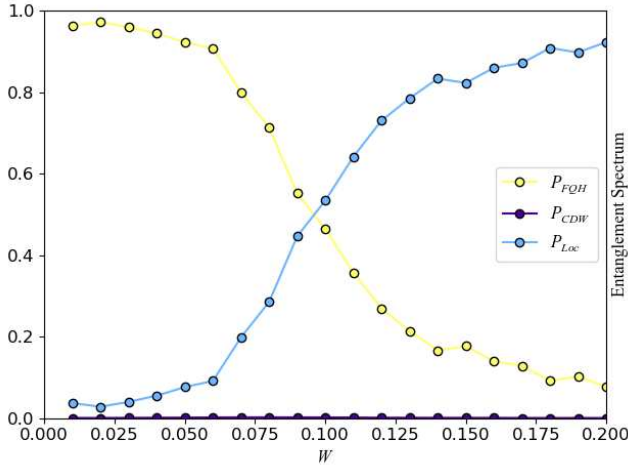
FIG. 8. The FQH-localized state transition at $\Delta V_1 = 0$. Neural network output probabilities of the system being in the FQH, CDW, and localized states (P_{FQH}, P_{CDW}, and P_{Loc} respectively) as a function of disorder strength W for $N_e = 6$ observed over $W \in [10^{-6}, 0.2]$ using the ES as input to the ANN. Phase transition to the localized state is predicted around $W = 0.095$, as was the case for $N_e = 5$.
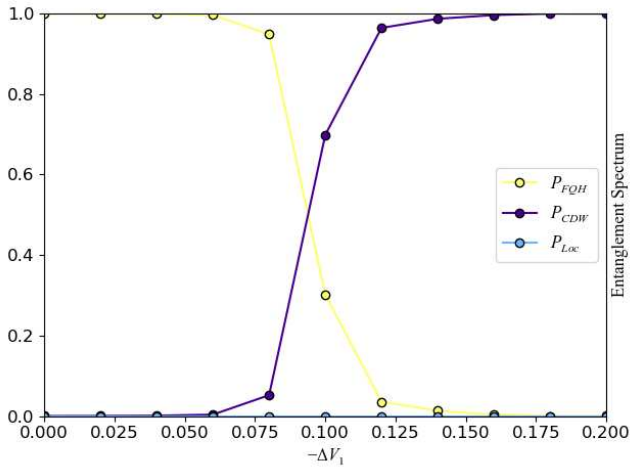

FIG. 9. The FQH-CDW transition along $W = 1 \times 10^{-6}$. Neural network output for probabilities of the system being in the FQH, CDW, and localized states (P_{FQH}, P_{CDW}, and P_{Loc}, respectively) as a function of pseudopotential shift ΔV_1 for $N_e = 6$ using the ES. Phase boundary appears around $-\Delta V_1 = 0.1$ as it does for $N_e = 5$.